Manipulating the electrical properties of conductive substoichiometric titanium oxides

Mehmet Gokhan Sensoy,[1,2,*] Robert W. Carpick,[1] David J. Srolovitz,[3] and Andrew M. Rappe[2,†]

[1]*Department of Mechanical Engineering and Applied Mechanics, University of Pennsylvania, Philadelphia, Pennsylvania 19104–6315, USA*

[2]*Department of Chemistry, University of Pennsylvania, Philadelphia, Pennsylvania 19104–6323, USA*

[3]*Department of Mechanical Engineering, The University of Hong Kong, Hong Kong SAR, China*

(Received 13 April 2023; revised 22 September 2023; accepted 18 January 2024; published 14 February 2024)

Conducting metal oxides offer many advantages for novel electronics applications, including sensors, fuel cells, piezoelectric devices, and microelectronic circuits, due to their conductivity, hardness, and chemically inert surfaces. In particular, their high electrical conductivity and mechanical properties make these materials suitable for microelectromechanical and nanoelectromechanical system (MEMS/NEMS) devices. NEMS switches have great potential for next-generation electronic computing associated with scalability to small dimensions, low power consumption, and (relatively) high speed. Oxygen-deficient Ti oxides with ordered planes of vacancies (Ti_nO_{2n-1}, Magnéli phases) are good candidates for NEMS applications because of their metallic conductivity, environmental resistance, and low cost, as compared with other conductive oxides like RuO_2. Although Ti suboxides have been produced in crystalline form, various synthesis methods may also produce amorphous material. In this paper, we focus on the structural and electrical transport properties of several Ti suboxides. In particular, we examine the effects of temperature, transition-metal dopants, and amorphization on these structural and electronic properties and the potential applicability of Magnéli phase Ti suboxides for NEMS switch applications.

DOI: 10.1103/PhysRevB.109.064106

I. INTRODUCTION

Transition-metal oxides exhibit electrical conductivities that vary over many orders of magnitude. This variability is attributable, in part, to a wide range of conduction mechanisms. Applications of these materials requiring high electrical conductivity focus, primarily, on those where electrical conduction is primarily metallic. While titanium dioxide (TiO_2) is a wide band-gap semiconductor, many of its substoichiometric variants, TiO_{2-x} or Ti_nO_{2n-1} for $n = 4 - 10$, are metallic conductors [1,2]. These variants, known as Magnéli phases [3–5], are determined by the ordered O vacancy planes named as shear planes [5–9]. The electrical conductivity of these suboxides depends on the structural phase and on both point defect and dopant concentrations. The large number of Magnéli phases and the ability to manipulate defect/dopant concentrations allows for electrical conductivity engineering in this class of materials.

The properties of rutile titanium dioxide (TiO_2) and its defect structures have been widely studied [10–22]. While rutile titanium dioxide is (nearly) a line compound, it remains stable when very slightly oxygen deficient (TiO_{2-x} for $x < 0.008$); the nonstoichiometry is accommodated by oxygen vacancies and/or titanium interstitials. Annealing TiO_2 under reducing conditions at high temperature (873–1273 K) can produce larger deviations from stoichiometry (larger x), leading to the formation of Magnéli phases (i.e., long-range ordered oxygen vacancy structures with $n = 4, 5,...$) [3,10,23,24]. From a theoretical and modeling point of view, it is known that, while TiO_2 is a typical semiconductor, Magnéli phases exhibit delocalized electrons in the d band, leading to a high electrical conductivity metallic conductor [6,7,25–27]. The Magnéli phases have a mixture of Ti^{+3} and Ti^{+4} oxidation states [26]. Electronic structure calculations have been used to understand mainly structural and electronic properties of crystalline Ti_4O_7 [7,25,26], Ti_5O_9 [27], and Ti_6O_{11} [8]. The concentration of delocalized charges is closely related to half the amount of O vacancies [22]. For example, the delocalized electrons in Ti_4O_7 reside in $Ti2O_3$ planes (with $Ti^{3.5+}$).

Among the Magnéli phase titanium suboxides, Ti_4O_7 has attracted the most attention, including for applications in lithium-sulfur batteries [28], photocatalysis [29], electrocatalysis [30], and thermoelectrics [31]. This phase has the highest electrical conductivity amongst the Magnéli phases and is degradation-resistant over a wide range of chemical environments [32]. The electrical conductivity of TiO_x ($0.75 \leqslant x \leqslant 1.45$), is reported to be 1000–3000 $(\Omega\,\mathrm{cm})^{-1}$. The reported room-temperature electrical conductivity of Ti_nO_{2n-1} is high for $n = 4$, 5, and 6 and decreases with increasing n [1]. The room-temperature electrical conductivity of bulk Ti_4O_7 [1] is 1605.3 $(\Omega\,\mathrm{cm})^{-1}$; this is within an order of magnitude of that of high-cost transition metal oxides (Ru, Ir, Re, and Rh) [33,34].

In electrical contact applications, electric current flows through contacting asperities at the interface, leading to a significant rise in local temperature, which can produce significant electrical conductivity changes in the critical contact

*Present address: Department of Physics, Recep Tayyip Erdogan University, 53100 Rize, Turkey; mgsensoy@seas.upenn.edu

†rappe@sas.upenn.edu

 ©2024 American Physical Society

region. The conductivity of Ti_nO_{2n-1} ($4 \leqslant n \leqslant 9$) varies with temperature (either increasing or decreasing with temperature, depending on the temperature range); this suggests that there may be conduction through different mechanisms [35]. For example, Ti_4O_7 shows two successive transitions in electrical conductivity (by increasing with temperature): from a low-temperature insulating phase to an intermediate phase (semiconductor-semiconductor transition) at 130 K, and from the intermediate phase to a high-temperature metallic phase (semiconductor-metal transition) at 150 K [1,2,35]. Similarly, the conductivities of both Ti_5O_9 and Ti_6O_{11} increase with increasing temperature for 150 K $< T <$ 300 K (semiconductor behavior) and decrease with increasing temperature above 450 K (metallic behavior).

Doping is an efficient strategy to modulate the electrical properties of metal oxides. For TiO_2, transition-metal (TM) dopants modify the structural and electronic properties (photocatalytic activity and electrical conductivity) [36–38] through modification of the band gap. For example, Ta and Nb doping shifts the Fermi level of TiO_2 into the conduction band, while Ru doping introduces Ru d electrons into the gap [39]. The conducting metal-oxide RuO_2 exhibits a large electrical conductivity [2.5×10^6 $(\Omega M)^{-1}$], which changes with TM doping [40]. TM doping of the highly conductive Magnéli phase of Ti_4O_7 can further increase the electrical conductivity beyond Ti_4O_7 (generating additional states near the Fermi energy). By doping Ti_nO_{2n-1}, properties relevant to its use as an electrode material can be altered, such as electrical [41,42], tribological [43,44], and electrocatalytic [45,46] characteristics. Doping Ti_4O_7 with metal cations such as Zr, Nb, Mo, and W increases both thermodynamic and structural stability [41,42]. It has been demonstrated that V and Fe doping in Ti_4O_7 stabilizes it against thermal oxidation and enhances the electrical conductivity due to an increase in the carrier concentration [41]. Doping Ti_4O_7 with Ce can improve catalytic activity and electrochemical stability via formation of surface oxygen vacancies compared to pristine Ti_4O_7 [45].

Compared to crystalline TM oxides, their amorphous counterparts exhibit some beneficial features, including lower deposition temperature, lower surface roughness, more uniform etching, increased flexibility, and the lack of grain boundaries and associated phenomena [47]. While crystalline metal oxides exhibit electronic and electrical properties that vary through the microstructure [48], this is not the case for the amorphous phases. The existence of several Ti-O Magnéli phases over a small composition range ($TiO_{1.75-1.9}$) suggests that amorphization may occur readily in these systems. The conductivities of the amorphous analogues of the Magnéli phases have not been reported.

Electrically conductive oxides are excellent candidates for low-resistance contacts in NEMS because of their wear resistance and resistance to a wide range of environmental degradation mechanisms that plague more traditional metallic contacts [49–51]. O-deficient substoichiometric phases of TiO_2 are appealing for such applications, owing to their metallic conductivity, environmental degradation resistance, and low cost compared with other conductive oxides [52,53].

In this paper, we examine the electrical and electronic behavior of several highly conductive Magnéli phases, Ti_nO_{2n-1} ($n = 4$, 5, and 6). In addition, we examine the effects of dopants, temperature, and amorphization in these systems. We focus on these questions: (1) What are the electronic structures and electrical properties of the different phases? (2) How do impurities affect these phases? (3) Since there are so many competing phases over a very small composition range in the Ti-O system, amorphous structures are possible. What are the properties of amorphous analogues of the Magnéli phases relative to their crystalline counterparts? Our study is based upon first-principles methods and the Kubo-Greenwood formalism [54,55] for calculating the electrical conductivity. Finite-temperature data are obtained through *ab initio* molecular dynamics (AIMD).

TABLE I. Structural parameters of TiO_2, Ti_4O_7, Ti_5O_9, and Ti_6O_{11} crystals. The atomic positions in TiO_2 were optimized using an on-site Ti d-state Hubbard U correction (U=4.2 eV) and a $5 \times 5 \times 8$ k-point mesh was employed for bulk rutile TiO_2 and a $5 \times 4 \times 3$ k-point mesh for bulk Ti_nO_{2n-1} ($n = 4, 5, 6$) with a 520 eV energy cutoff.

	Theory (this paper) / Experiment			
Parameter	r-TiO_2 [67]	Ti_4O_7 [68]	Ti_5O_9 [68]	Ti_6O_{11} [68]
a (Å)	4.70/4.58	5.56/5.59	5.61/5.62	5.60/5.58
b (Å)	4.69/4.58	6.93/6.90	7.21/7.18	7.21/7.14
c (Å)	3.04/2.95	7.21/7.13	8.55/8.56	9.80/9.69
α (°)	90.0/90.0	64.05/64.12	69.38/69.49	90.03/89.75
β (°)	90.0/90.0	72.01/71.24	74.98/75.19	79.64/79.38
γ (°)	90.0/90.0	75.28/75.65	71.17/71.31	71.23/71.5
Space group	$P4_2/mnm$	P$\bar{1}$[2]	P$\bar{1}$[2]	P$\bar{1}$[2]
Crystal system	tetragonal	trigonal	trigonal	trigonal

II. COMPUTATIONAL DETAILS

Our calculations were performed using the density functional theory package VASP [56,57] in the generalized gradient approximation with the Perdew-Burke-Ernzerhof exchange correlation energy functional [58]. The Fermi surface was Gaussian smeared, and the core electrons were treated via the projector augmented-wave method [59,60]. The energy cutoff was 520 eV for the plane-wave basis in the structure optimization with a relatively dense k-point mesh of $3 \times 3 \times 3$ for the $2 \times 2 \times 2$ supercells of Ti_4O_7, Ti_5O_9 and Ti_6O_{11} crystal structures. For the 216-atom supercell of crystalline rutile-TiO_2 (r-TiO_2), we used a $2 \times 2 \times 3$ k-point mesh. The crystalline rutile TiO_2 and Ti_nO_{2n-1} ($n = 4$, 5, and 6) structural parameters are in Table I.

To describe the strong electron correlation interactions in the d orbitals of the Ti 3d electrons, the DFT+U method [61,62] is introduced for the inclusion of on-site Coulomb repulsion at atomic sites. The results presented in this paper are from GGA+U with U=4 eV for Ti 3d electrons. For clarity, we also compared the low-temperature (at 120 K) and high-temperature (at 300 K) phases of Ti_4O_7. The low T phase with GGA+U [63] (see Fig. S1 [64]) is shown to be a semiconductor (0.27 eV), in agreement with experimental band gap value of 0.25 eV [65]. The high T phase (same composition, different ion arrangement) with GGA+U is shown to be very

metallic (agrees with experiment) [1–4,25,26]. Our choice (GGA) is justified by previous experimental and theoretical results [63,65,66] showing the metallic behavior of Magnéli phases, Ti_nO_{2n-1} ($n = 4$, 5, and 6), at high temperatures.

A melt and quench method was used to generate 216, 176, 224, and 272 atom amorphous variants of the TiO_2, Ti_4O_7, Ti_5O_9, and Ti_6O_{11} crystal structures, respectively. The liquid Ti suboxide structures were generated computationally by AIMD of the crystal at 4000 K for times sufficient to lose structural memory, and then quenching to and annealing at 0, 300, 600, and 900 K for 45 ps (9000 5-fs AIMD time steps) under isothermal-isobaric conditions (NPT) [69]. For computational efficiency, we employed relatively low-precision settings (Γ point only; plane-wave kinetic-energy cutoff of 400 eV) in the AIMD simulations. After equilibration, atomic structures were collected following 15 ps thermalization in 1.5 ps intervals. For each configuration, we performed static density functional theory calculations with a denser k-point grid ($3 \times 3 \times 3$); we used Fermi-Dirac function smearing to obtain the frequency-dependent electrical conductivity (see Supplemental Material [64] for details). The widths of the Dirac delta function (Eq. (S1) [64]) were selected from average values of eigenvalue differences of each configuration.

The electrical conductivity values (σ_0) were obtained by averaging over structures generated using AIMD simulations. The σ_0 values were extracted from $\sigma(\omega)$ by calculating $\sigma_0 = \lim_{\omega \to 0} \sigma(\omega)$. We fit $\sigma(\omega)$ to a Drude model [70,71] to obtain electrical conductivity values at 0 eV (see Fig. S2 [64]). The three diagonal components of the dc conductivity ($\sigma_{0,xx}$, $\sigma_{0,yy}$, $\sigma_{0,zz}$) were calculated; the reported dc conductivity is the arithmetic average of these.

In addition to studying the defect-free crystal structures of the suboxides, we also considered the role of point defects. Specifically, the structure and energetics of dopant additions were examined, starting from crystalline Ti_4O_7. The effects of TM doping of Ti_4O_7 were determined by substitution of a single dopant for a Ti atom in a $2 \times 2 \times 2$ supercell (i.e., $Ti_{63}M_1O_{112}$, where M=V, Nb, Ta, Zr, Cr, Mo, and Sc), corresponding to a ≈1.6% doping concentration. The defect formation energy and the doping energy (heat of solution) H_F is defined as

$$H_F = E_d - E_s - \sum_i \mu n_i, \tag{1}$$

where E_d is the total energy of the defective or doped structure, E_s is the total energy of the pure, stoichiometric structure, n_i is number of dopant atoms in the unit cell, and μ_i is the chemical potential of species i. The dopants considered were Nb, Ta, V, Mo, Zr, Sc, and Cr.

III. CRYSTALLINE SUBOXIDES

Previous experimental studies [1] reported that the first Ti_4O_7 Magnéli phase has the highest conductivity [1830 $(\Omega\,\mathrm{cm})^{-1}$] and that the electrical conductivity of Ti_nO_{2n-1} decreases with increasing n. For example, the room temperature electrical conductivity of Ti_5O_9 ($n = 5$) and Ti_6O_{11} ($n = 6$) are 1540 and 1100 $(\Omega\,\mathrm{cm})^{-1}$, respectively. Our predicted results (see Table II) slightly overestimate the experimental values, but the trend of the electrical conductivity is consistent with previous reported values [1]. The small supercell sizes and discretization of the eigenvalues can be the main sources of error in the results [72].

TABLE II. Electrical conductivities (σ_0) of a supercell containing $2 \times 2 \times 2$ trigonal simulation cells of Ti_4O_7, Ti_5O_9, and Ti_6O_{11} at 0 K and 300 K. Prefixes c- and a- denote crystal and amorphous (see text), respectively.

Structure	0 K	300 K	600 K	900 K	300 K exp. [73]
c-Ti_4O_7	2113	2093	1974	1850	1830
a-Ti_4O_7	1340	1378	1497	1505	
c-Ti_5O_9	1787	1526	1558	1537	1540
a-Ti_5O_9	1153	1171	1247	1251	
c-Ti_6O_{11}	1586	1410	1445	1436	1100
a-Ti_6O_{11}	960	1067	1057	1097	

Due to the metallic nature of the Ti $n = 4$–6 suboxides, increasing temperature from 0 K to 300 K leads to a decrease in electrical conductivity. For c-Ti_4O_7, we found no significant effect of temperature on the predicted electrical conductivity below 300 K but 12% reduction upon increasing temperature from 300 K to 900 K (see Table II). This trend was only observed at low temperature for c-Ti_5O_9 and c-Ti_6O_{11} (see Table II).

IV. TRANSITION METAL DOPING

In the Ti_4O_7 Magnéli phase (bulk crystal), there are two inequivalent Ti sites present as Ti^{3+} and Ti^{4+}, as seen in Fig. 1(a), and these two sites are bonded to six O^{2-} ions in

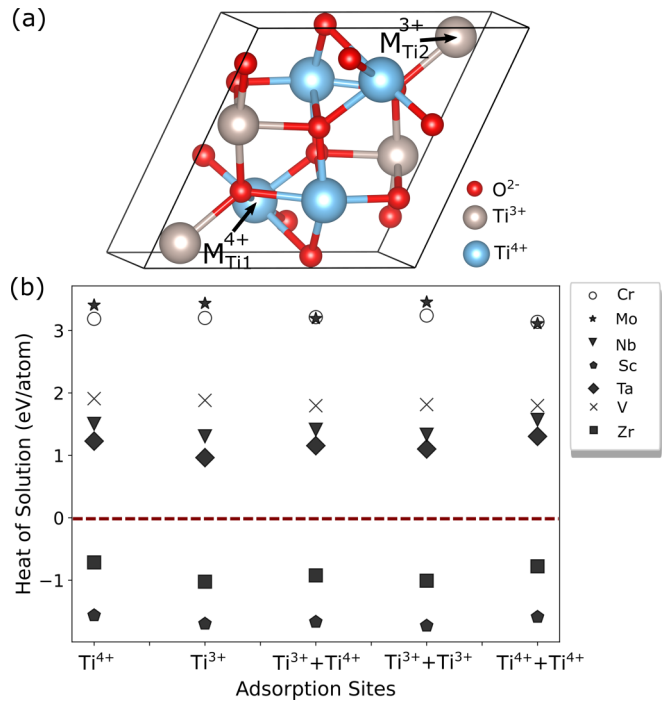

FIG. 1. (a) Doping sites in Ti_4O_7 Magnéli phase. (b) Heat of solution, H_F (eV/atom) for transition-metal dopants in Ti_4O_7(M_{Ti}, M= Nb, Ta, Zr, V, Sc, Cr, and Mo.) at Ti^{3+}, Ti^{4+}, $Ti^{3+} + Ti^{3+}$ ($2M_{Ti}^{3+}$), $Ti^{4+} + Ti^{4+}$ ($2M_{Ti}^{4+}$), and $Ti^{3+} + Ti^{4+}$ sites.

TABLE III. Bader charge of dopant, ρ (|e|), density of states at the Fermi energy, $N(E_F)$ (states/eV) and predicted electrical conductivity, σ_0 ($(\Omega\,\mathrm{cm})^{-1}$) of $Ti_{3.94}M_{0.06}O_7$ (doping concentration is 1.6%, M= Nb, Ta, Zr, V, Sc, Cr, and Mo).

Dopant	ρ	$N(E_F)$	σ_0
undoped		74	2113.0
Nb	2.52	140.4	3046.1
Ta	2.51	133.41	3027.3
Zr	2.51	120.9	2974.0
V	1.62	94.8	2951.7
Sc	1.77	118.5	2914.2
Cr	1.38	103.7	2861.8
Mo	1.39	87.5	2765.9

the form of TiO_6 octahedra that share corners with equivalent TiO_6 octahedra. The bond distances range from 1.94–2.08 Å and 1.88–2.18 Å for Ti^{3+}–O^{2-} and Ti^{4+}–O^{2-}, respectively. To find the most favorable doping site in Ti_4O_7, we calculated the heat of solution for each doping element at Ti^{3+} and Ti^{4+} sites. The results are shown in Fig. 1(b).

For $M_{0.5}Ti_{3.5}O_7$ (M=Nb, Ta, Zr, V, Sc, Cr, and Mo), the Ti^{4+} site is the most favorable for Cr and Mo, while Ti^{3+} is the most favorable for Nb, Sc, Ta, V, and Zr [see Fig. 1(b)]. Overall, the most suitable TMs with which to dope Ti_4O_7 are Sc, Zr, Nb, and Ta since they have the lowest heats of solution (and it is negative for Sc and Zr). For electrical conductivity enhancement, both Ti^{3+} and Ti^{4+} sites are very similar (see Table S1 [64]). For example, the predicted electrical conductivity value for $Nb_{Ti^{3+}}$ is only 1% higher than $Nb_{Ti^{4+}}$. Moreover, we studied pairs of metal dopants in Ti_4O_7 at different pairs of doping sites, namely, $2M_{Ti^{3+}}$, $2M_{Ti^{4+}}$, $M_{Ti^{3+}}$, $+ M_{Ti^{4+}}$. We found that the $2M_{Ti^{3+}}$ site (doping concentration $\approx$25%) is the most favorable of the three possibilities for Nb, Sc, Ta, and Zr, while the $2M_{Ti^{4+}}$ site is the most favorable for Cr and Mo. The $Ti^{3+} + Ti^{4+}$ site is preferable for only for V.

Our Bader charge analysis [74,75] for the Nb, Ta, Zr, V, Sc, Cr, and Mo doped structures (see Table III) suggests that the maximum charge donation occurs for Nb, Ta, and Zr doping. As a result of charge donation by these elements, the phase stability increases; this may be associated with the strengthening of the overall chemical bonding. On the contrary, Cr injects less charge, leading to reduced chemical bonding and hence decreased phase stability. Transferring and also sharing electrons between anions and cations (ionic and covalent bonding nature) leads to bond strengthening. While minor changes were observed in the vicinity of O atoms (e.g., metal-O bond length), the overall effect of these chemical bonding changes can be seen in the heat of solution data.

Although Ta doping fulfills the increased phase stability criterion (according to the heat of solution), a projected density of states analysis (PDOS) shows that Nb exhibits the largest DOS at the Fermi level (140.4 states/eV) when incorporated into c-Ti_4O_7. For the Ta- and Zr-doped structures, the $N(E_F)$ values were found to be 133.4 and 120.9 states/eV, respectively. Compared to stoichiometric Ti_4O_7, Nb doping leads to 50% increase in the electrical conductivity, while Ta and Zr doping lead to 44.7% and 42.1% increases, respectively. For Sc and Cr doping, we found that the magnitude of $N(E_F)$ values are not consistent with the σ_0 values. This may be associated with the effect of magnetization on the electrical properties (discussed further below). The results are summarized in Table III. Overall, $N(E_F)$ and the conductivity σ_0 are higher in the doped cases than for stoichiometric Ti_4O_7.

The PDOS for the undoped and all doped Ti_4O_7 cases are shown in Fig. 2. The PDOS profiles for Nb-, Ta-, Zr-, and Sc-doped Ti_4O_7 are very similar to one another. The TM dopant d states have a large spatial overlap with other states. Therefore, the contribution to the Fermi level is relatively smaller. For example, the contribution of Nb doping to the DOS at the Fermi level is higher than that for Zr doping due to a stronger overlap with states at the Fermi level. This may be evidence of delocalization of d-orbital electrons as a result of atomic distortion in the vicinity of the doping center (see Fig. S3 [64]). On the contrary, for Cr, Mo, and V doping, we observed localization of d states below the Fermi level and in the pseudogap (i.e., O 2p–Mo 4d hybridization). Although, $N(E_F)$ is expected to decrease by this localization, $N(E_F)$ increases, as summarized in Table III. This is associated with transferring additional electrons to the surrounding anions (O atoms) from dopant atoms in doped Ti_4O_7. As the distortion of the atomic structure around the doping center promotes delocalization of d-orbital electrons, $N(E_F)$ increases compared with stoichiometric Ti_4O_7.

The classical theory of electrical conductivity of metals suggests that increasing $N(E_F)$ gives rise to an increase in the predicted electrical conductivity. As just discussed and shown in Table III, this behavior is consistent with our simulation results. This is important because the states near the Fermi energy determine most electronic properties (e.g., conductivity); only electrons with energies close to the Fermi level participate in electrical conduction in metals. This suggests that increasing the number of free electrons leads to higher electronic density at the Fermi level, resulting in conductivity enhancement in metals. While the effects of TM doping on electrical conductivity (see Table III) is relatively weak as compared with doping effects on the conductivity in semiconductors [37,38], we do see that all of the TM dopants increase the electrical conductivity.

The dopant effect on the electron density distribution is illustrated through delocalization of electron probability density in contour electron localization function (ELF) plots in Figs. 3(a) and 3(b). The O atoms are clearly seen as effective centers for localization of valence electrons from the reference bare structure in Fig. 3(a). Figure 3(b) (and for other TM doping of Ti_4O_7 in Fig. S3 [64]) shows the ELF contour plot for the Nb_{Ti} structure. In this case, the electronic charge is mostly localized by the ELF value of nearly 0.7 in defect site. More importantly, the 0.3 ELF value between the Nb and nearest-neighbor O atoms due to the charge transfer from Nb to O is evidence of charge delocalization as a result of the atomic structure distortion around the impurity site, compared to the undoped Ti_4O_7. This additional delocalized electron density is consistent with the enhanced electrical conductivity observed for doped Ti_4O_7. This is because the local distortion of the atomic structure accompanying the electron delocalization is associated with the dopants donating their valence electrons.

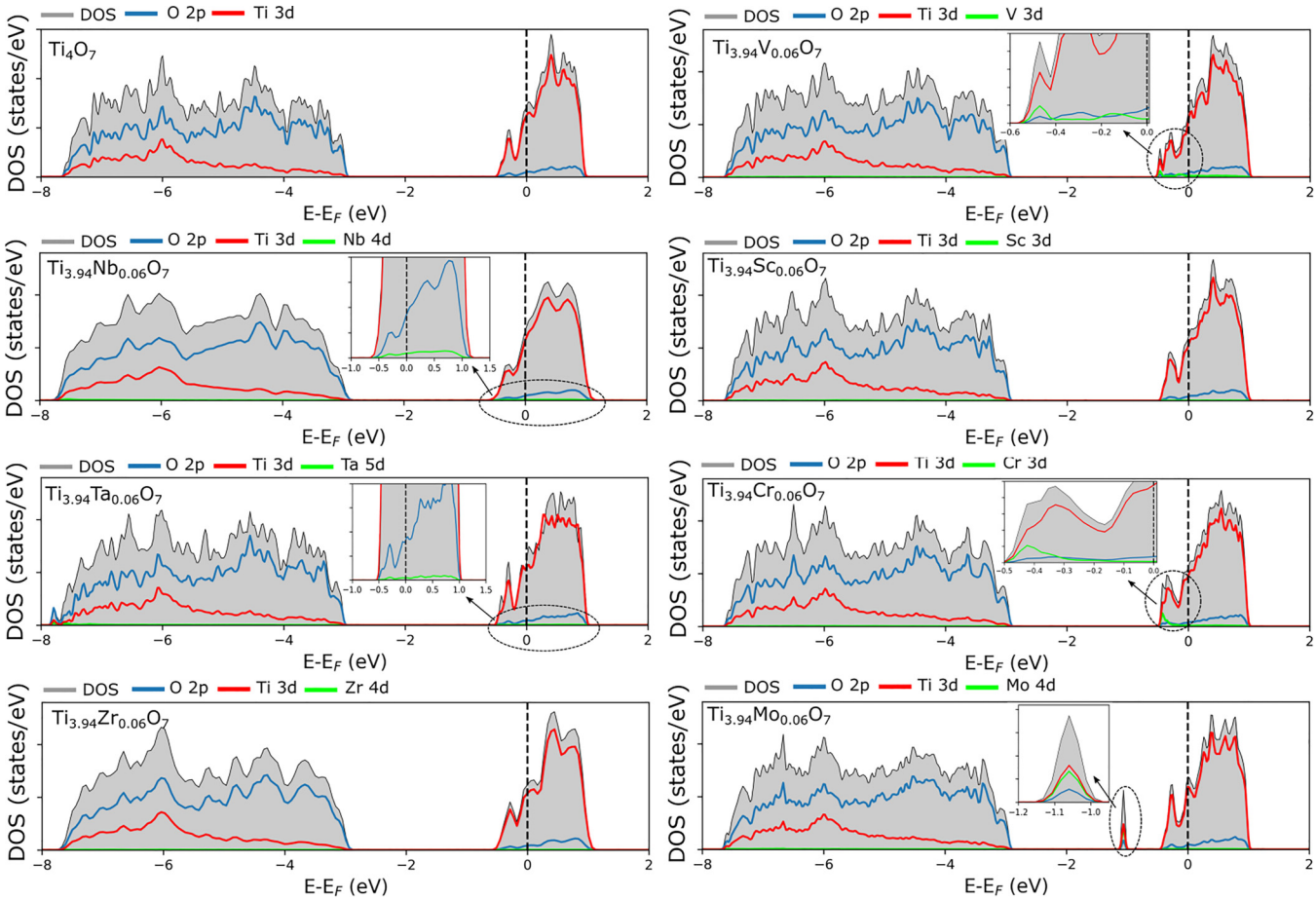

FIG. 2. The projected density of states (PDOS) of $Ti_{3.94}M_{0.06}O_7$ (transition metal dopants, M = Nb, Ta, Zr, V, Sc, Cr, Mo). The Fermi energy is set to zero. Insets are enlargements of the circled sections of the PDOS plots. The gray regions are the total density of states and the blue, red, and green curves correspond to the O 2p, Ti 3d, and M d states, respectively.

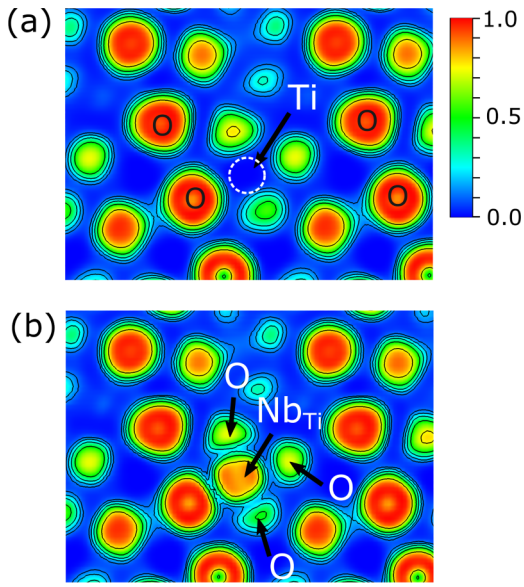

FIG. 3. The electron localization function (ELF) contours of (a) undoped and (b) Nb-doped Ti_4O_7, $Ti_{3.98}Nb_{0.02}O_7$. ELF values of 1, 0.5, and 0 correspond to perfect localization, metallic (free electron) regions, and regions of zero electron density, respectively.

These results suggest that Ta and Nb are the most promising transition-metal dopants for enhancing the electrical conductivity and phase stability of Ti_4O_7. We then calculated the change of the electrical conductivity (σ_0) as a function of metal dopant (Nb, Ta, Zr, V, Sc, Cr, and Mo) concentration (Fig. 4 and Fig. S4 [64]). These results demonstrate that the conductivity values increases monotonically with increasing Ta and Nb concentration, while it decreases for Sc, Zr, V, Cr, and Mo.

Our DOS analysis shows that the DOS at the Fermi level increases with increasing TM doping. For example, $N(E_F)$ increases from 59.4 to 101.2 to 147.1 states/eV when the Nb concentration is increased from 0 to 1.6 to 12.5%. Correspondingly, the electrical conductivity increases by ≈44% and ≈64.8% for the same Nb-doping concentrations. This clearly shows that increasing $N(E_F)$ values leads to an increase in the predicted electrical conductivity.

Interaction of metal-doped Ti_4O_7 with oxygen vacancies and interstitials was also considered to regulate the electronic structure of Ti_4O_7. Our results show that different metal substitutions could lead to different thermodynamic stability depending on the oxidation states of defect site and the metal dopant. When the Ti^{3+} and/or Ti^{4+} sites are replaced by a metal dopant (Nb, Ta, Zr, V, Sc, Cr, and Mo), oxygen vacancies or interstitials will be generated to retain the charge

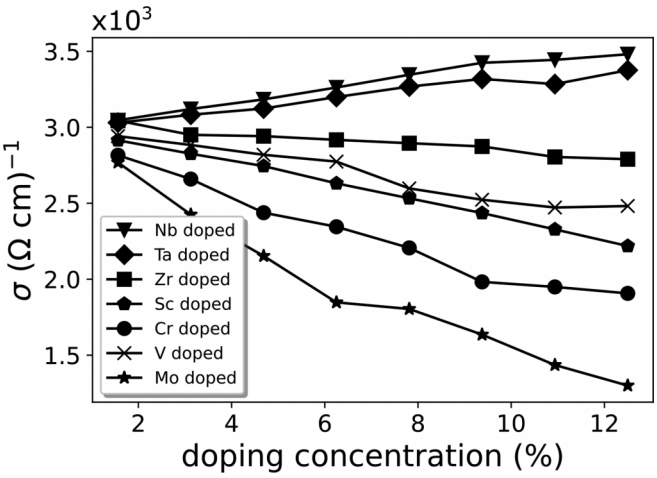

FIG. 4. The electrical conductivity as a function of dopant concentration in Ti_4O_7, $Ti_{4-n}M_nO_7$, M=Nb, Ta, Zr, V, Sc, Cr, and Mo.

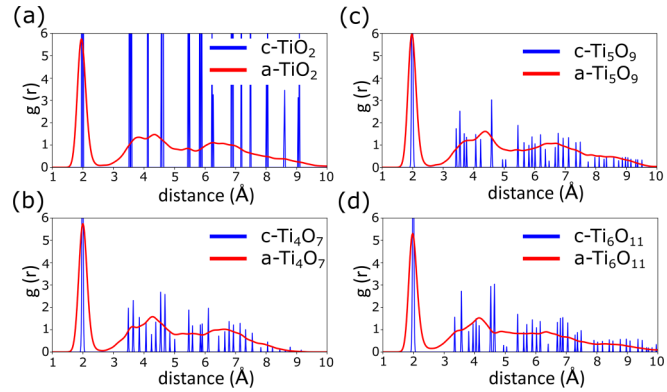

FIG. 5. The Ti-O radial distribution functions $g(r)$ for amorphous (a) TiO_2, (b) Ti_4O_7, (c) Ti_5O_9, and (d) Ti_6O_{11} at 300 K and their crystalline counterparts at 0 K.

neutrality in doped Ti_4O_7. Then, the local lattice distortion will trigger the electron redistribution in doped Ti_4O_7 to optimize the electronic structure. To identify the most stable site for vacancy and interstitial formation, multiple oxygen sites of the metal-doped structures were considered, and we show Ti^{3+} and Ti^{4+} sites with oxygen vacancy and interstitial sites in bulk Ti_4O_7 (see Fig. S5 [64]). Gibbs formation energies were calculated from the following equations:

$$E_{\text{form}} = E(M_{x\text{Ti}4-x}O_{7\mp y}) - E(M_x\text{Ti}_{4-x}O_7) \pm \frac{N_O}{2}(E_{O_2} - \Delta\mu O_2), \quad (2)$$

where $E(M_x\text{Ti}_{4-x}O_{7-y})$ and $E(M_x\text{Ti}_{4-x}O_{7+y})$ are the total energy of dopants in Ti_4O_7 with oxygen vacancy and interstitial; $E(M_x\text{Ti}_{4-x}O_7)$ is the energy of dopant in Ti_4O_7. $\pm$ N_O is the number of oxygen vacancy/ interstitial atom in $M_x\text{Ti}_{4-x}O_{7\mp y}$, E_{O_2} is the DFT energy of the O_2 molecule, and $\Delta\mu_{O_2}$ is applied to convert the chemical potential of molecular oxygen at 300 K and 1 atm. The formation energies of oxygen vacancy and interstitial for each dopant are plotted in Fig. S6 [64].

The O incorporation thermodynamically stabilizes the Nb, Ta, Zr, and Sc dopants. It can be achieved by one O interstitial per one metal atom introduced for Ta, Zr, and Sc, while there are two O interstitials for Nb. At very low chemical potential of O, the O vacancy becomes thermodynamically favorable. We found that the V, Cr, and Mo doping will not promote the incorporating of O in Ti_4O_7 compared to the undoped Ti_4O_7, while the O vacancy formation is favorable at low oxygen chemical potential region. We then calculated the change of the electrical conductivity (σ_0) as a function of oxygen vacancy/interstitial concentration for doped Ti_4O_7 (Fig. S7 [64]) These results demonstrate that the conductivity values decrease with oxygen incorporation, while the oxygen vacancy slightly increase the conductivity. Our results support the conclusion that minor Nb doping provides a promising path for enhancing the electrical conductivity of Ti_4O_7. However, incorporation of extra oxygen in Nb-, Ta-, Zr-, and Sc-doped Ti_4O_7 decreases the conductivity.

V. AMORPHOUS SUB-OXIDES

The existence of several Magnéli Ti suboxides with very similar formation energies (within 0.01 eV/atom) in a very small composition range suggests that disorder is expected to be very common. This disorder could include amorphous phase formation or disordered vacancies on the (crystalline) oxygen sublattice. The extend of disorder will be sensitive to synthesis conditions. Here we examine and contrast two well-defined cases: ordered Magnéli suboxide phases and disordered suboxides due to rapid computational quenching of the TiO_2, Ti_4O_7, Ti_5O_9, and Ti_6O_{11} suboxides from the liquid state to low temperature.

The four crystalline oxides were computationally heated to 4000 K, melted, and equilibrated in their liquid form, followed by quenches to 900, 600, and 300 K within 40 ps, annealed at those temperatures for 20 ps, and then cooled to 0 K (each in 10 ps) using AIMD. While it is difficult to estimate quench rates during film deposition, the ones employed here are surely fast compared with most experimental synthesis techniques [76]; high quench rates were employed for computational efficiency. The evolution of the system energies (per atom) during the quench and anneal processes are shown in Fig. S8 [64]; the absence of abrupt drops in the energy and examination of the atomic structure suggest that no crystallization occurs during cooling/annealing. The Ti-O radial distribution functions $g(r)$ of the amorphous structures (compositions corresponding to TiO_2, Ti_4O_7, Ti_5O_9, and Ti_6O_{11}) at the end of the 300 K thermal schedule along with their crystalline counterparts at 0 K are shown in Fig. 5. Smooth $g(r)$ distributions were obtained by time averaging the atomic coordinate data. These results suggest that these suboxides formed by rapid quenching from the melt are amorphous rather than crystalline with oxygen vacancy disorder.

The Ti–Ti, O–O, and Ti–O bond nearest-neighbor distances and $g(r)$ in the amorphous structures (see Fig. S9 [64]) are very closely related to those in their crystalline counterparts.

In addition, the nearest-neighbor Ti–O distances in all of the amorphous sub-oxides show sharp peaks centered at approximately 2.0 Å, which is the single-crystal TiO_2 nearest-neighbor separation [see Fig. 5(a)]. Nonetheless, there is a

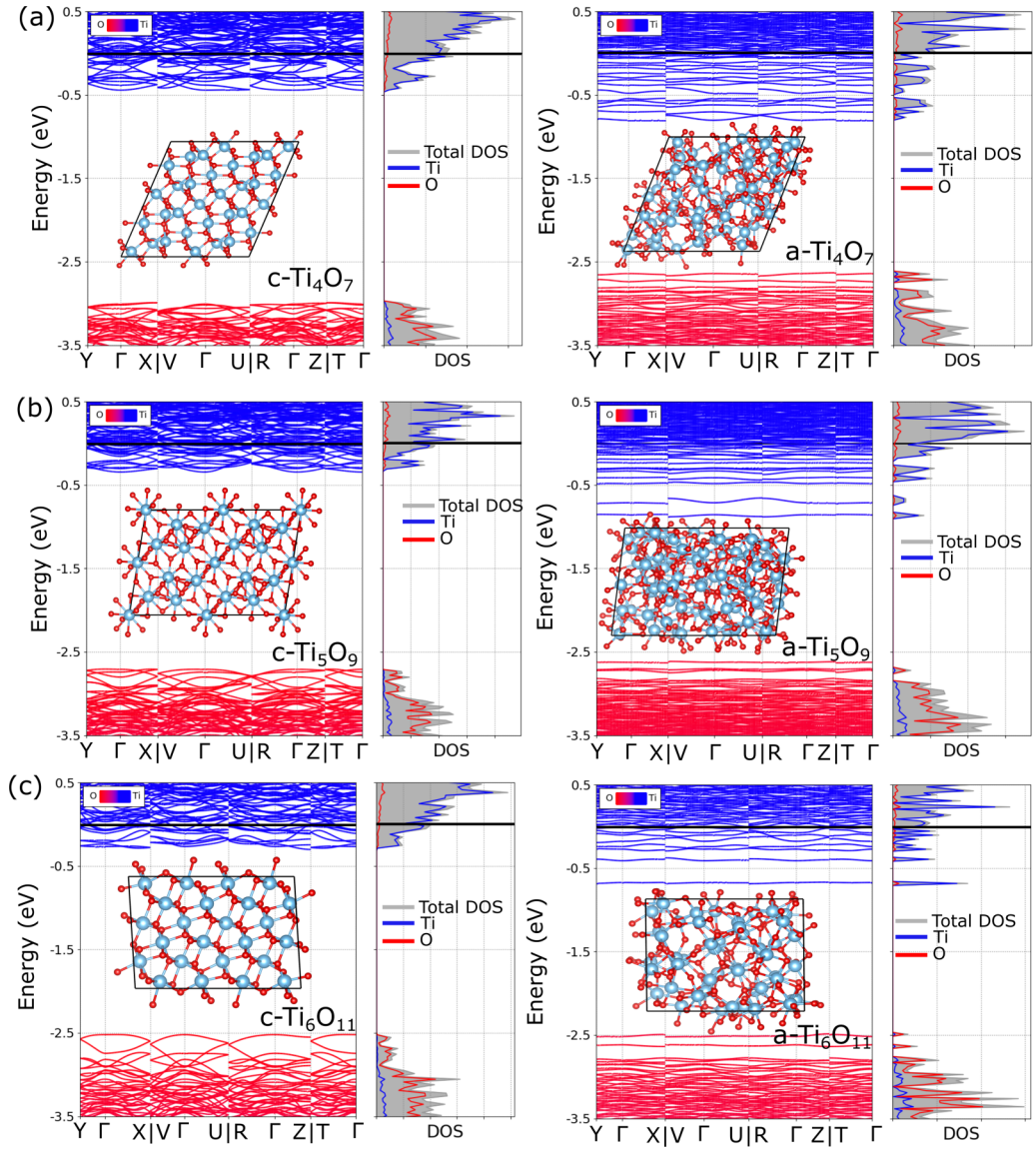

FIG. 6. Electronic band structure and density of states of crystalline and amorphous (a) Ti_4O_7 (176-atom supercell), (b) Ti_5O_9 (224-atom supercell), and (c) Ti_6O_{11} (136-atom supercell). The Fermi energy is set to zero. Insets show the crystal structures. Blue and red spheres represent titanium and oxygen, respectively. The gray regions in the density of state plots correspond to the total density of states, while the blue and red curves represent Ti and O states, respectively.

very small increase in the nearest-neighbor Ti–O distance (2.01 Å) in the amorphous suboxides as compared with their crystalline counterparts (1.98 Å). The second major Ti–O peak in $g(r)$ for the amorphous suboxides occur at ≈4.2 Å. These observations are consistent with the similarities between the atomic structures of amorphous versions of TiO_2, Ti_4O_7, Ti_5O_9, and Ti_6O_{11}.

In the amorphous structures of the Magnéli and rutile phase compositions, most Ti atoms are surrounded by six oxygen atoms (as in their crystalline form) and most O atoms have three titanium atom neighbors (in the crystalline Magnéli phases, O atoms have two or three Ti neighbors). However, some Ti have five and seven O neighbors, and some O have two or four Ti neighbors. This observation is consistent with previous experimental and theoretical studies for amorphous TiO_2 (we know of no such data for Ti suboxide compositions) [77]. The lower oxygen coordination number suggests both variations in local short-range order and is also consistent with the observed reduction in the Ti–O distance in the amorphous structures.

The electrical conductivity reduces significantly upon amorphization, as shown in Table II. For example, the conductivity of a-Ti_4O_7 is ≈33% lower than its corresponding crystalline form. Nonetheless, the band structures and the density of states plots in Fig. 6 suggest that the conductivity is metallic (the Fermi energy lies midband) in both the crystalline and amorphous forms.

According to the electronic band structures of amorphous phases in Fig. 6, there is a set of flat bands corresponding to localized electronic states as a result of disordering. These flat

bands below the Fermi level have a very small dispersion, as evidenced by the shapes of the corresponding peaks in the DOS. In addition to these flat bands, dispersive bands were observed around the Fermi level, corresponding to the delocalized states in crystalline structure. The DOS plots in Fig. 6 showed that amorphization leads to a small broadening of the DOS and the development of states within the pseudogap below the Fermi level. These localize O and Ti states lie below the Fermi energy level, thereby lowering the electrical conductivity of the amorphous phases.

The localization associated with disordering gives rise to a decrease in the predicted electrical conductivity as summarized in Table II. Some electrons located on the Ti cation transfer to the O anion due to its larger electronegativity by preserving the energy differences between the Ti-3*d* and the O-2*p* states. Therefore, the disorder-induced defect levels upon amorphization, which appear below the rest of the *d* bands near Fermi level, can trap electrons, leading to small changes in the electrical conductivity [78]. Note that amorphization leads to drops of up to 40% in the electrical conductivity.

VI. DISCUSSION

Defective TiO_{2-x} has a higher ionic contribution to electrical current compared to stoichiometric TiO_2 [79,80]. For example, oxygen vacancies in TiO_{2-x} are ionized and serve as mobile space charges due to the delocalized vacancy states. In that case, reordering/creation of defects in the structure can switch between the different available phases like conductive Magnéli phases. For this reason, understanding the relationship between defects, oxide phase behavior, and conductivity induced by changes in growth conditions will be a key factor. For example, the Magnéli phases can be synthesized using scalable methods like atomic layer deposition of amorphous TiO_x on a substrate; this allows highly precise thickness control, high uniformity, and low defect density [81,82]. Alternatively, the crystalline Ti oxides can be heated to higher temperatures ($>$ 1000 K) under a controlled atmosphere to synthesize Ti suboxides with a Magnéli phase [83,84]. For device applications, we expect that Magnéli phases can be grown by precisely controlling the oxygen pressure and temperature in the atmosphere [83,85–88] using TiO_2 and/or amorphous TiO_x as a source.

The results presented above suggest that the electrical properties of the Magnéli phases of Ti suboxides can be manipulated by structural phase changes and transition-metal doping. In particular, TM-doping was found to be an efficient strategy to increase the electrical conductivity.

Although trends in the predicted electrical conductivity in the crystalline materials are consistent with previously reported values, they slightly overestimate those reported experimentally. This may be due to defects (e.g., impurities or high conductivity paths in the microstructure) in the experimental samples or the discretization of the eigenvalues resulting from the small supercell sizes in the simulations. Our preliminary investigation suggests that the supercell size effect is not significant for the conductivity; e.g., the Ti_4O_7 σ_0 of a $2 \times 2 \times 1$ unit-cell size (88-atoms) supercell was found to be only ≈9% lower than that of the $2 \times 2 \times 2$ (176-atoms) supercell.

The existence of several distinct titanium suboxide conductive Magnéli crystal structures (Ti_nO_{2n-1}; $n = 4,5,6,...$) of very similar energies and compositions suggest the strong possibility that amorphous structures will readily form, depending on synthesis conditions. Since our motivation to consider these Magnéli phases is based upon their high electrical conductivity, it is notable that amorphization leads to a significant reduction of their electrical conductivity. The defect energy levels formed up on complete amorphization lead to free electron trapping and localization that decrease the electrical conductivity. Nonetheless, electrical conduction in the amorphous structures, like their crystalline counterparts, is primarily metallic (based on electronic structural analysis). Amorphous metallic conductors generally have a higher resistivity than the corresponding crystalline structures due to the shorter mean free path of electrons [89–92]. Hence, the predicted electrical conductivity values would be expected to decrease as temperature increases.

In general, since oxides tend to have high melting points (1940 K for Ti_4O_7 [93]), the electrical conductivity is less temperature dependent than pure metals [94]. Moreover, this is particularly important for MEMS/NEMS switches where the electrical current density is very high across asperity contacts; high current density leads to high temperatures. Our findings suggest that the changes in the electrical conductivity for both crystalline (i.e., +12.5% for c-Ti_4O_7) and especially amorphous (i.e., −12.3% for a-Ti_4O_7) Ti suboxides are small over the entire temperature range examined $0 \leqslant T$ (K) $\leqslant$ 900. Hence, we consider both amorphous and crystalline Ti suboxides of potential interest for MEMS/NEMS switch applications. Overall, our expectations are that, while lower, the electrical conductivity of amorphous Ti suboxides is still sufficiently high for use in NEMS contact applications. For these applications, mechanical properties and chemical activity are important. Therefore, further study is required to evaluate these properties for the Magnéli phases and amorphous Ti suboxides.

VII. SUMMARY AND CONCLUSION

We presented a detailed *ab initio* study of the structural, electronic, and electrical transport properties of the Magnéli Ti suboxides (Ti_nO_{2n-1}). We demonstrated how the electrical properties may be manipulated through phase amorphization, substitutional doping, and temperature changes. To predict the finite temperature electrical conductivity properties, we coupled the Kubo-Greenwood approach with atomic structures obtained via AIMD simulations. Although the predicted electrical conductivity for the stoichometric Ti sub-oxides are higher than experimental measurement, the conductivity trends are consistent with experimental observations. TM doping was found to provide an effective means of manipulating the electrical properties of Ti_4O_7. We found that even small doping (≈1%) leads to large electrical conductivity enhancements (≈40%); larger doping concentrations have little effect on electrical conductivity. This small doping effect is associated with electron delocalization. On the contrary, higher doping concentrations promote electron localization which

decreases electrical conductivity. We expect that the same trend applies for Ti_5O_9 and Ti_6O_{11}.

ACKNOWLEDGMENTS

M.G.S. and R.W.C. acknowledge support from the National Science Foundation (NSF) under Grant No. CMMI-1854702, a LEAP HI project entitled "Ultra-Low Power Computing: A Disruptive Approach Through a New Integrated Nanomechanics Framework". A.M.R. acknowledges support from the Department of Energy, Office of Science, Office of Basic Energy Sciences, under Grant No. DE-SC0019281. D.J.S. gratefully acknowledges the support of the Hong Kong Research Grants Council Collaborative Research Fund C1005-19G. Computational resources were provided by XSEDE (Grant No. TG-DMR120073).

[1] R. F. Bartholomew and D. R. Frankl, Electrical properties of some titanium oxides, Phys. Rev. **187**, 828 (1969).

[2] L. Degiorgi, P. Wachter, and C. Schlenker, Study of the metal-insulator transition in Ti_4O_7 by optical investigations, Phys. B: Condens. Matter **161**, 341 (1990).

[3] S. Andersson, B. Collen, U. Kuylenstierna, and A. Magnéli, Phase analysis studies on the titanium-oxygen system, Acta Chem. Scand. **11**, 1641 (1957).

[4] B. Xu, H. Y. Sohn, Y. Mohassab, and Y. Lan, Structures, preparation and applications of titanium suboxides, RSC Adv. **6**, 79706 (2016).

[5] A. Kumar, N. H. Barbhuiya, and S. P. Singh, Magnéli phase titanium sub-oxides synthesis, fabrication and its application for environmental remediation: Current status and prospect, Chemosphere **307**, 135878 (2022).

[6] A. C. M. Padilha, J. M. Osorio-Guillén, A. R. Rocha, and G. M. Dalpian, Ti_nO_{2n-1} Magnéli phases studied using density functional theory, Phys. Rev. B **90**, 035213 (2014).

[7] A. C. M. Padilha, H. Raebiger, A. R. Rocha, and G. M. Dalpian, Charge storage in oxygen deficient phases of TiO_2: Defect physics without defects, Sci. Rep. **6**, 28871 (2016).

[8] S. Harada, K. Tanaka, and H. Inui, Thermoelectric properties and crystallographic shear structures in titanium oxides of the Magnèli phases, J. Appl. Phys. **108**, 083703 (2010).

[9] Q. Zhang, W. Liu, Y. Zhou, J. Li, T. Sun, Q. Liu, Y. Ma, J. Wang, J. Li, R. Zhao, Y. Sui, T. Matsumoto, N. Muroyama, A. Yamano, K. D. M. Harris, Z. J. Shen, and O. Terasaki, Andersson-Magnéli phases Ti_nO_{2n-1}: Recent progress inspired by Swedish scientists, Chemie Z. Anorg. Allg. Chem. **647**, 126 (2021).

[10] L. Bursill and B. Hyde, Crystallographic shear in the higher titanium oxides: Structure, texture, mechanisms and thermodynamics, Prog. Solid State Chem. **7**, 177 (1972).

[11] C. Tang, D. Zhou, and Q. Zhang, Synthesis and characterization of Magnéli phases: Reduction of TiO_2 in a decomposed NH_3 atmosphere, Mater. Lett. **79**, 42 (2012).

[12] R. Phillips, P. Hansen, and E. Eisenbraun, Atomic layer deposition fabricated substoichiometric TiO_x nanorods as fuel cell catalyst supports, J. Vac. Sci. Technol. **30**, 01A125 (2011).

[13] E. Verrelli and D. Tsoukalas, Cluster beam synthesis of metal and metal-oxide nanoparticles for emerging memories, Solid-State Electron. **101**, 95 (2014).

[14] M. Wajid Shah, Y. Zhu, X. Fan, J. Zhao, Y. Li, S. Asim, and C. Wang, Facile synthesis of defective TiO_{2-x} nanocrystals with high surface area and tailoring bandgap for visible-light photocatalysis, Sci. Rep. **5**, 15804 (2015).

[15] H. Iwasaki, N. Bright, and J. Rowland, The polymorphism of the oxide Ti_3O_5, J. Less-Common Met. **17**, 99 (1969).

[16] R. Roy and W. B. White, Growth of titanium oxide crystals of controlled stoichiometry and order, J. Cryst. Growth **13**, 78 (1972).

[17] Q. Pang, D. Kundu, M. Cuisinier, and L. F. Nazar, Surface-enhanced redox chemistry of polysulphides on a metallic and polar host for lithium-sulphur batteries, Nat. Commun. **5**, 4759 (2014).

[18] B. Xu, D. Zhao, H. Y. Sohn, Y. Mohassab, B. Yang, Y. Lan, and J. Yang, Flash synthesis of Magnéli phase (Ti_nO_{2n-1}) nanoparticles by thermal plasma treatment of H_2TiO_3, Ceram. Int. **44**, 3929 (2018).

[19] D. Portehault, V. Maneeratana, C. Candolfi, N. Oeschler, I. Veremchuk, Y. Grin, C. Sanchez, and M. Antonietti, Facile general route toward tunable Magnéli nanostructures and their use as thermoelectric metal oxide/carbon nanocomposites, ACS Nano **5**, 9052 (2011).

[20] S.-S. Huang, Y.-H. Lin, W. Chuang, P.-S. Shao, C.-H. Chuang, J.-F. Lee, M.-L. Lu, Y.-T. Weng, and N.-L. Wu, Synthesis of high-performance titanium sub-oxides for electrochemical applications using combination of sol–gel and vacuum-carbothermic processes, ACS Sustainable Chem. Eng. **6**, 3162 (2018).

[21] T. Ioroi, H. Kageyama, T. Akita, and K. Yasuda, Formation of electro-conductive titanium oxide fine particles by pulsed UV laser irradiation, Phys. Chem. Chem. Phys. **12**, 7529 (2010).

[22] A. F. Arif, R. Balgis, T. Ogi, F. Iskandar, A. Kinoshita, K. Nakamura, and K. Okuyama, Highly conductive nano-sized Magnéli phases titanium oxide (TiO_x), Sci. Rep. **7**, 3646 (2017).

[23] J. Anderson and A. Khan, Equilibria of intermediate oxides in the titanium-oxygen system, J. Less-Common Met. **22**, 219 (1970).

[24] G. Wang, Y. Liu, J. Ye, X. Yang, and Z. Lin, Formation mechanism of Ti_4O_7 phase prepared by carbothermal reduction reaction, J. Am. Ceram. Soc. **103**, 3871 (2020).

[25] X. Zhong, I. Rungger, P. Zapol, and O. Heinonen, Electronic and magnetic properties of Ti_4O_7 predicted by self-interaction-corrected density functional theory, Phys. Rev. B **91**, 115143 (2015).

[26] L. Liborio, G. Mallia, and N. Harrison, Electronic structure of the Ti_4O_7 Magnéli phase, Phys. Rev. B **79**, 245133 (2009).

[27] I. Slipukhina and M. Ležaić, Electronic and magnetic properties of the Ti_5O_9 Magnéli phase, Phys. Rev. B **90**, 155133 (2014).

[28] H. Wei, E. F. Rodriguez, A. S. Best, A. F. Hollenkamp, D. Chen, and R. A. Caruso, Chemical bonding and physical trapping of sulfur in mesoporous Magnéli Ti_4O_7 microspheres for high-performance Li–S battery, Adv. Energy Mater. **7**, 1601616 (2017).

[29] M. Toyoda, T. Yano, B. Tryba, S. Mozia, T. Tsumura, and M. Inagaki, Preparation of carbon-coated Magnéli phases Ti_nO_{2n-1}

and their photocatalytic activity under visible light, Appl. Catal. B **88**, 160 (2009).

[30] S. Liang, H. Lin, X. Yan, and Q. Huang, Electro-oxidation of tetracycline by a Magnéli phase Ti_4O_7 porous anode: Kinetics, products, and toxicity, Chem. Eng. J. **332**, 628 (2018).

[31] S. Conze, A. Poenicke, H.-P. Martin, A. Rost, I. Kinski, J. Schilm, and A. Michaelis, Manufacturing processes for TiO_x-based thermoelectric modules: From suboxide synthesis to module testing, J. Electron. Mater. **43**, 3765 (2014).

[32] J. R. Smith, F. C. Walsh, and R. L. Clarke, Electrodes based on Magnéli phase titanium oxides: the properties and applications of Ebonex® materials, J. Appl. Electrochem. **28**, 1021 (1998).

[33] R. A. Matula, Electrical resistivity of copper, gold, palladium, and silver, J. Phys. Chem. Ref. Data **8**, 1147 (1979).

[34] G. K. White and S. B. Woods, Thermal and electrical conductivity of rhodium, iridium, and platinum, Can. J. Phys. **35**, 248 (1957).

[35] K. Szot, M. Rogala, W. Speier, Z. Klusek, A. Besmehn, and R. Waser, TiO_2—a prototypical memristive material, Nanotechnology **22**, 254001 (2011).

[36] A. Khlyustova, N. Sirotkin, T. Kusova, A. Kraev, V. Titov, and A. Agafonov, Doped TiO_2: the effect of doping elements on photocatalytic activity, Mater. Adv. **1**, 1193 (2020).

[37] L. R. Sheppard, T. Bak, and J. Nowotny, Electrical properties of niobium-doped titanium dioxide. 1. Defect disorder, J. Phys. Chem. B **110**, 22447 (2006).

[38] M. A. Alim, T. Bak, A. Atanacio, J. D. Plessis, M. Zhou, J. Davis, and J. Nowotny, Electrical conductivity and defect disorder of tantalum-doped TiO_2, J. Am. Ceram. Soc. **100**, 4088 (2017).

[39] E. Dy, R. Hui, J. Zhang, Z.-S. Liu, and Z. Shi, Electronic conductivity and stability of doped titania ($Ti_{1-X}M_XO_2$, M = Nb, Ru, and Ta)—A density functional theory-based comparison, J. Phys. Chem. C **114**, 13162 (2010).

[40] D. Music, F. H.-U. Basse, and J. M. Schneider, Quantum mechanically guided design of transition metal alloyed RuO_2 nanorods, Cryst. Growth Des. **10**, 4531 (2010).

[41] J. T. English and D. P. Wilkinson, The superior electrical conductivity and anodic stability of vanadium-doped Ti_4O_7, J. Electrochem. Soc. **168**, 103509 (2021).

[42] T. Yuan, N. Jin, W. Cheng, Y. Yun, X. Tian, L. Wang, and J. Ye, Insight into the stability in cation substitution of Magnéli phase Ti_4O_7, Appl. Phys. Lett. **121**, 214101 (2022).

[43] M. N. Gardos, Magnéli phases of anion-deficient rutile as lubricious oxides. Part II. Tribological behavior of Cu-doped polycrystalline rutile (Ti_nO_{2n-1}), Tribol. Lett. **8**, 79 (2000).

[44] D. Calestani, F. Licci, E. Kopnin, G. Calestani, A. Gauzzi, F. Bolzoni, T. Besagni, V. Boffa, and M. Marezio, Preparation and characterization of powders and crystals of $V_{n-x}Ti_xO_{2n-1}$ Magnéli oxides, Cryst. Res. Technol. **40**, 1067 (2005).

[45] H. Lin, R. Xiao, R. Xie, L. Yang, C. Tang, R. Wang, J. Chen, S. Lv, and Q. Huang, Defect engineering on a Ti_4O_7 electrode by Ce^{3+} doping for the efficient electrooxidation of perfluorooctanesulfonate, Environ. Sci. Technol. **55**, 2597 (2021).

[46] J. Maragatha and S. Karuppuchamy, Microwave synthesis of C-doped Ti_4O_7 for photocatalytic applications, Adv. Sci. Eng. Med. **10**, 1085 (2018).

[47] A. G. Revesz and F. P. Fehlner, The role of noncrystalline films in the oxidation and corrosion of metals, Oxid. Met. **15**, 297 (1981).

[48] S. R. Elliott, The structure of amorphous materials, in *Properties and Applications of Amorphous Materials*, edited by T. M.F. and T. L. (Springer, Dordrecht, 2001), Vol. 9.

[49] T. Yokokawa, T. Yano, C. Kawakita, K. Hinohara, and A. Nagai, A study on the surface deactivation treatment of rhodium-plated contact reed switches, IEEE Trans. Compon., Hybrids, Manuf. Technol. **9**, 124 (1986).

[50] F. Streller, G. E. Wabiszewski, D. B. Durham, F. Yang, J. Yang, Y. Qi, D. J. Srolovitz, A. M. Rappe, and R. W. Carpick, Novel materials solutions and simulations for nanoelectromechanical switches, in 2015 IEEE 61st Holm Conference on Electrical Contacts (Holm, San Diego, CA, USA, 2015), pp. 363–369.

[51] P. G. Slade, *Reed Switches* (CRC Press, Boca Raton, 1999), pp. 535–572.

[52] W. W. Jang, J. O. Lee, J.-B. Yoon, M.-S. Kim, J.-M. Lee, S.-M. Kim, K.-H. Cho, D.-W. Kim, D. Park, and W.-S. Lee, Fabrication and characterization of a nanoelectromechanical switch with 15-nm-thick suspension air gap, Appl. Phys. Lett. **92**, 103110 (2008).

[53] H. Kam, Y. Chen, and T.-J. K. Liu, Reliable micro-electromechanical (mem) switch design for ultra-low-power logic, in 2013 IEEE International Reliability Physics Symposium (IRPS) (Monterey, CA, USA, 2013), pp. 6A.1.1–6A.1.5.

[54] R. Kubo, Statistical-mechanical theory of irreversible processes. I. General theory and simple applications to magnetic and conduction problems, J. Phys. Soc. Jpn. **12**, 570 (1957).

[55] D. A. Greenwood, The Boltzmann equation in the theory of electrical conduction in metals, Proc. Phys. Soc. **71**, 585 (1958).

[56] G. Kresse and J. Furthmüller, Efficiency of *ab-initio* total energy calculations for metals and semiconductors using a plane-wave basis set, Comput. Mater. Sci. **6**, 15 (1996).

[57] G. Kresse and J. Hafner, *Ab initio* molecular dynamics for liquid metals, Phys. Rev. B **47**, 558 (1993).

[58] J. P. Perdew, K. Burke, and M. Ernzerhof, Generalized gradient approximation made simple, Phys. Rev. Lett. **77**, 3865 (1996).

[59] P. E. Blöchl, Projector augmented-wave method, Phys. Rev. B **50**, 17953 (1994).

[60] G. Kresse and D. Joubert, From ultrasoft pseudopotentials to the projector augmented-wave method, Phys. Rev. B **59**, 1758 (1999).

[61] V. I. Anisimov, J. Zaanen, and O. K. Andersen, Band theory and Mott insulators: Hubbard *U* instead of Stoner *I*, Phys. Rev. B **44**, 943 (1991).

[62] S. L. Dudarev, G. A. Botton, S. Y. Savrasov, C. J. Humphreys, and A. P. Sutton, Electron-energy-loss spectra and the structural stability of nickel oxide: An LSDA+*U* study, Phys. Rev. B **57**, 1505 (1998).

[63] L. Liborio and N. Harrison, Thermodynamics of oxygen defective Magnéli phases in rutile: A first-principles study, Phys. Rev. B **77**, 104104 (2008).

[64] See Supplemental Material at http://link.aps.org/supplemental/10.1103/PhysRevB.109.064106 for a detailed explanation of dc conductivity prediction, for figures with electron localization function (ELF) contours of un-doped and TM-doped Ti_4O_7, metal doping sites in Ti_4O_7, oxygen vacancy and interstitial positions, calculated Gibbs free formation energies, and predicted electrical conductivity values as a function of oxygen concentration in metal doped Ti_4O_7, evolution of the system energy in AIMD simulation, and Ti-Ti and O-O radial distribution functions for amorphous structures, and for tables with

predicted electrical conductivity for doped Ti_4O_7 at different atomic sites.

[65] D. Kaplan, C. Schlenker, and J. J. Since, Optical absorption and metal-insulator transitions in Ti_4O_7, Philos. Mag. **36**, 1275 (1977).

[66] A. D. Inglis, Y. L. Page, P. Strobel, and C. M. Hurd, Electrical conductance of crystalline Ti_nO_{2n-1} for n=4–9, J. Phys. C **16**, 317 (1983).

[67] J. K. Burdett, T. Hughbanks, G. J. Miller, J. W. Richardson, and J. V. Smith, Structural-electronic relationships in inorganic solids: Powder neutron diffraction studies of the rutile and anatase polymorphs of titanium dioxide at 15 and 295 K, J. Am. Chem. Soc. **109**, 3639 (1987).

[68] A. Afir, M. Achour, and N. Saoula, X-ray diffraction study of Ti-O-C system at high temperature and in a continuous vacuum, J. Alloys Compd. **288**, 124 (1999).

[69] E. Hernàndez, Metric-tensor flexible-cell algorithm for isothermal–isobaric molecular dynamics simulations, J. Chem. Phys. **115**, 10282 (2001).

[70] M. P. Desjarlais, J. D. Kress, and L. A. Collins, Electrical conductivity for warm, dense aluminum plasmas and liquids, Phys. Rev. E **66**, 025401(R) (2002).

[71] M. Pozzo, M. P. Desjarlais, and D. Alfè, Electrical and thermal conductivity of liquid sodium from first-principles calculations, Phys. Rev. B **84**, 054203 (2011).

[72] R. J. Bondi, M. P. Desjarlais, A. P. Thompson, G. L. Brennecka, and M. J. Marinella, Electrical conductivity in oxygen-deficient phases of tantalum pentoxide from first-principles calculations, J. Appl. Phys. **114**, 203701 (2013).

[73] J. Houlihan, W. Danley, and L. Mulay, Magnetic susceptibility and EPR spectra of titanium oxides: Correlation of magnetic parameters with transport properties and composition, J. Solid State Chem. **12**, 265 (1975).

[74] G. Henkelman, A. Arnaldsson, and H. Jónsson, A fast and robust algorithm for Bader decomposition of charge density, Comput. Mater. Sci. **36**, 354 (2006).

[75] W. Tang, E. Sanville, and G. Henkelman, A grid-based Bader analysis algorithm without lattice bias, J. Phys.: Condens. Matter **21**, 084204 (2009).

[76] S. Asalzadeh and K. Yasserian, The effect of various annealing cooling rates on electrical and morphological properties of TiO_2 thin films, Semiconductors **53**, 1603 (2019).

[77] H. Zhang, B. Chen, J. F. Banfield, and G. A. Waychunas, Atomic structure of nanometer-sized amorphous TiO_2, Phys. Rev. B **78**, 214106 (2008).

[78] H.-X. Deng, S.-H. Wei, S.-S. Li, J. Li, and A. Walsh, Electronic origin of the conductivity imbalance between covalent and ionic amorphous semiconductors, Phys. Rev. B **87**, 125203 (2013).

[79] M. K. Nowotny, T. Bak, and J. Nowotny, Electrical properties and defect chemistry of TiO_2 single crystal. I. Electrical conductivity, J. Phys. Chem. B **110**, 16270 (2006).

[80] T. Leichtweiss, R. A. Henning, J. Koettgen, R. M. Schmidt, B. Holländer, M. Martin, M. Wuttig, and J. Janek, Amorphous and highly nonstoichiometric titania (TiO_x) thin films close to metal-like conductivity, J. Mater. Chem. A **2**, 6631 (2014).

[81] J. Aarik, K. Kukli, A. Aidla, and L. Pung, Mechanisms of suboxide growth and etching in atomic layer deposition of tantalum oxide from $TaCl_5$ and H_2O, Appl. Surf. Sci. **103**, 331 (1996).

[82] D.-H. Kwon, K. M. Kim, J. H. Jang, J. M. Jeon, M. H. Lee, G. H. Kim, X.-S. Li, G.-S. Park, B. Lee, S. Han, M. Kim, and C. S. Hwang, Atomic structure of conducting nanofilaments in TiO_2 resistive switching memory, Nat. Nanotechnol. **5**, 148 (2010).

[83] H. Malik, S. Sarkar, S. Mohanty, and K. Carlson, Modelling and synthesis of Magnéli phases in ordered titanium oxide nanotubes with preserved morphology, Sci. Rep. **10**, 8050 (2020).

[84] S. Siracusano, V. Baglio, C. D'Urso, V. Antonucci, and A. Aricò, Preparation and characterization of titanium suboxides as conductive supports of IrO_2 electrocatalysts for application in SPE electrolysers, Electrochim. Acta **54**, 6292 (2009).

[85] K. Yoshimatsu, O. Sakata, and A. Ohtomo, Superconductivity in Ti_4O_7 and γ-Ti_3O_5 films, Sci. Rep. **7**, 12544 (2017).

[86] M. Matsuda, Y. Yamada, Y. Himeno, K. Shida, M. Mitsuhara, and M. Matsuda, Magnéli Ti_4O_7 thin film produced by stepwise oxidation of titanium metal foil, Scr. Mater. **198**, 113829 (2021).

[87] A. Kumar, N. H. Barbhuiya, K. Jashrapuria, N. Dixit, C. J. Arnusch, and S. P. Singh, Magnéli-phase Ti_4O_7-doped laser-induced graphene surfaces and filters for pollutant degradation and microorganism removal, ACS Appl. Mater. Interfaces **14**, 52448 (2022).

[88] X. Tao, J. Wang, Z. Ying, Q. Cai, G. Zheng, Y. Gan, H. Huang, Y. Xia, C. Liang, W. Zhang, and Y. Cui, Strong sulfur binding with conducting Magnéli-phase Ti_nO_{2n-1} nanomaterials for improving lithium–sulfur batteries, Nano Lett. **14**, 5288 (2014).

[89] E. William Cowell, Amorphous multi-component metals as electrode materials, Master's thesis, 2010, Oregon State University, Electrical and Computer Engineering, Oregon State.

[90] A. H. Committee, *Materials Characterization* (American Society for Metals, Materials Park, OH, USA, 1998), Vol. 10.

[91] N. F. Mott, *Conduction in Non-Crystalline Materials* (Oxford University Press, Oxford, 1993).

[92] J. Dugdale, *The Electrical Properties of Disordered Metals* (Cambridge University Press, Cambridge, 2005).

[93] R. Tu, G. Huo, T. Kimura, and T. Goto, Preparation of Magnéli phases of $Ti_{27}O_{52}$ and Ti_6O_{11} films by laser chemical vapor deposition, Thin Solid Films **518**, 6927 (2010).

[94] P. Neudeck, R. Okojie, and L.-Y. Chen, High-temperature electronics: A role for wide bandgap semiconductors? Proc. IEEE **90**, 1065 (2002).